Surface restoration of polycrystalline Sb_2Se_3 thin films by conjugated molecules enabling high-performance photocathodes for photoelectrochemical water splitting

Jeiwan Tan[a], Wooseok Yang[b], Hyungsoo Lee[a], Jaemin Park[a], Kyungmin Kim[a], Oliver S. Hutter[c], Laurie J. Phillips[d], Sanggi Shim[a], Juwon Yun[a], Youngsun Park[a], Jeongyoub Lee[a], Jonathan D. Major[d], Jooho Moon[a]

[a] *Department of Materials Science and Engineering, Yonsei University, 50 Yonsei-ro Seodaemun-gu Seoul 03722, Republic of Korea*
[b] *Department of Chemistry, University of Zurich, Zurich 8057, Switzerland*
[c] *Department of Mathematics, Physics and Electrical Engineering, Northumbria University, Newcastle upon Tyne, UK*
[d] *Stephenson Institute for Renewable Energy, Physics Department, University of Liverpool, Liverpool L69 7ZF, UK*

Keywords: Onset potential, Photocurrent density, Buried junction, Defect passivation, Conjugated amino acid

Abstract: Achieving both high onset potential and photocurrent in photoelectrodes is a key challenge while performing unassisted overall water splitting using tandem devices. We propose a simple interface modification strategy to maximize the performance of polycrystalline Sb_2Se_3 photocathodes for photoelectrochemical (PEC) water splitting. The *para*-aminobenzoic acid (PABA) modification at Sb_2Se_3/TiO_2 interface enhanced both the onset potential and photocurrent of the Sb_2Se_3 photocathodes. The surface defects in the polycrystalline Sb_2Se_3 limited the photovoltage production, lowering the onset potential of the photocathode. Surface restoration using the conjugated PABA molecules efficiently passivated the surface defects on the Sb_2Se_3 and enabled the rapid photoelectron transport from the Sb_2Se_3 to the TiO_2 layer. The PABA treated Sb_2Se_3 photocathode exhibited substantially improved PEC performance; the onset potential increased from 0.35 to 0.50 V compared to the reversible hydrogen electrode (V_{RHE}), and the photocurrent density increased from 24 to 35 mA cm^{-2} at 0 V_{RHE}.

1. Introduction

Photoelectrochemical (PEC) water splitting is one of the most promising pathways to convert solar energy into chemical energy stored in H_2 [1]. In order to achieve a high solar-to-hydrogen (STH) conversion efficiency, both high photocurrent density (J_{ph}) and photovoltage (V_{ph}) of photoelectrodes are required. Although 1.23 V is thermodynamically required to split water into H_2 and O_2, a higher V_{ph} should be achieved to compensate for significant potential losses during the practical PEC reactions, including potential losses for charge transport within the photoelectrode and the overpotentials for electrochemical reactions at the electrode/electrolyte interface [2,3]. As the STH efficiency is proportional to the J_{ph} given the sufficient V_{ph} to drive the water splitting reactions, many researchers have developed various strategies for maximizing the J_{ph} while producing sufficiently large V_{ph} [4].

One critical strategy for enhancing the performance of photoelectrodes is an interface engineering, which is a general term referring to all strategies to heterogeneous semiconductor into the interface is inapplicable to general photoelectrodes as it highly depends on the material's combination and requires specific band positions depending on the light absorbers. Even when an ideal combination of two materials in terms of band alignment is considered, the deposition of the *n*-type layer might suffer from instability issues caused by inter-diffusion of constituent atoms during full device fabrication [14]. Moreover, the prediction of the maximum V_{ph} based on the band alignment assumes homogeneous interfaces. However, those are unachievable in practical polycrystalline thin films with non-ideal factors such as the presence of pin-holes, surface defects, and surface roughness. Thus, some interface engineering strategies with the addition of semiconductor layers often result in a significant reduction in J_{ph} despite the slightly enhanced V_{ph} [7,13].

It was also reported that the insertion of a molecular dipole layer at the interface of the *p*- and *n*-type materials can shift the relative band position to enhance the V_{ph} [15,16]. Wick-Joliat et al. recently elucidated that the insertion of phosphonic acid dipole layer at Si/TiO_2 can significantly improve the onset potential of Si photocathode up to 400 mV as supported by both theoretical calculation and experimental observation [17]. However, the dipole layer deposition was largely influenced by the surface quality, so that the dipole layer strategy is likely effective only on a high-quality semiconductor such as single-crystalline Si, as evidenced by the relatively small improvement in polycrystalline semiconductor interfaces such as Sb_2Se_3/TiO_2 (~ 40 mV) and Cu_2O/TiO_2 (~ 70 mV). Typically, the surface defects of polycrystalline semiconductor induce poor interface quality when overlayer is deposited, leading to the band mismatch and playing a role as recombination center, which in turn causes the losses for charge transport through the interface [18,19]. Treating the surface of polycrystalline material with thin organic molecular layers such as self-assembly monolayers (SAM, *e.g.*, (3-aminopropyl)triethoxysilane) has been considered as one possible strategy to passivate the interface defects and to improve the V_{ph} and efficiency in photovoltaic applications [20,21], but they have not been widely applied to PEC devices. It has been only used for the purpose of attaching photo-active organic molecules (*e.g.*, fullerene derivatives) onto the surface of electrodes [22, 23]. Therefore, it is still required to develop a simple interface modification strategy for high performance PEC devices, which can be effectively applied to non-ideal semiconductors having a rough surface, pin-holes and surface defects.

Herein, by taking Sb_2Se_3/TiO_2/Pt photocathode as a reference device, we propose a simple interface modification strategy in which the Sb_2Se_3/TiO_2 interface is decorated with a conjugated organic molecule, *para*-aminobenzoic acid (PABA). Polycrystalline Sb_2Se_3 thin film, deposited by close space sublimation method, was selected as a light absorber that has been considered as a promising less toxic and low-cost semiconductor for efficient PEC water splitting, whereas TiO_2 was employed as a *p-n* junction partner as well as a physical protection layer [7,24]. The PABA is solution-processable and cost-effective amino acid which has been introduced in PV application to enhance the efficiency by reducing trap states and promoting charge extraction [25,26]. Without the PABA treatment, large fluctuation of the surface potential in Sb_2Se_3 thin films was observed due to the presence of pin-holes and surface defects, while the relatively uniform distribution of surface potential was shown after the PABA treatment. We demonstrated that the surface restoration of polycrystalline Sb_2Se_3 film with ring-containing amino acids (either conjugated and non-conjugated ones) prevented the formation of

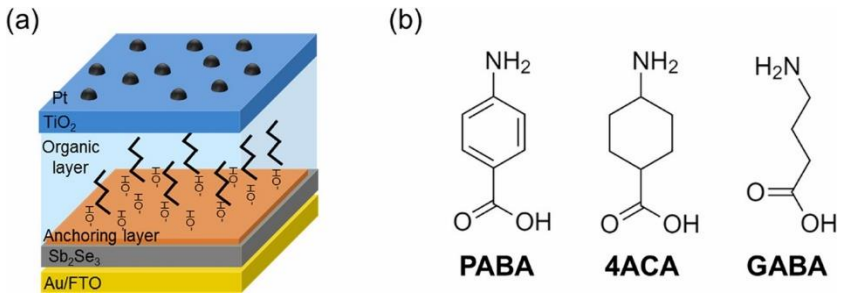

Fig. 1. (a) Schematic illustration of the photocathodes in the FTO/Au/Sb_2Se_3/AL/organic layer/TiO_2/Pt configuration (not to scale); (b) Molecular structure of the three amino acids used as the organic layers.

interface state at Sb_2Se_3/TiO_2 junction, while the J_{ph} is highly amplified only in the presence of conjugated PABA molecules. As a result, upon a simple PABA treatment at Sb_2Se_3/TiO_2 interface, not only the J_{ph} at 0 V_{RHE} increased by ~ 1.5 times, but also the onset potential positively shifted from 0.35 up to 0.5 V_{RHE}. Characterizing the photoelectron behaviour as a function of applied potential *via* the electrochemical impedance spectroscopy (EIS) and intensity-modulated photocurrent spectroscopy (IMPS) confirmed that the PABA layer enabled the rapid charge transport from Sb_2Se_3 to TiO_2 particularly near the onset potential region. Our study provides a simple and effective interface treatment strategy to maximize the PEC performance of photocathodes for PEC water splitting.

2. Experimental section

2.1. Preparation of Sb_2Se_3 thin films

Sb_2Se_3 films were deposited onto FTO/Au substrate *via* the close space sublimation (CSS) process using a home-made CSS system as described in our previous report [7,27]. Briefly here, a compact layer was grown from stoichiometric Sb_2Se_3 (Alfa Aesar, 99.999 % metals basis) using a source temperature of 365 °C and a substrate temperature of 320 °C for 10 min at a pressure of 0.05 mbar. Subsequently, the deposition was completed using a source temperature of 470 °C for 15 min and a pressure of 13 mbar. These films were quickly cooled down to room temperature under N_2 flow of 5 L min^{-1} as turning the heater off. *2.2. Anchoring/organic layer deposition*

All precursors, *para*-aminobenzoic acid (PABA, Sigma Aldrich), 4-aminocyclohexanecarboxylic acid (4ACA, Sigma Aldrich) and γ-aminobutyric acid (GABA, Sigma Aldrich) were dissolved in DI water and sonicated for 15 min to make transparent precursor solutions. The concentration of each solution was 2 mM otherwise mentioned. Prior to the deposition of organic layers, an anchoring layer was deposited onto as-fabricated Sb_2Se_3 thin films by the atomic layer deposition (ALD, Lucida D100, NCD Inc.). The ALD process was carried out at 120 °C using tetrakis(dimethylamino)titanium (TDMAT) and H_2O as Ti and O sources, respectively. Ten cycles were repeated, yielding amorphous TiO_2 films with a thickness of ~ 0.6 nm (0.59 Å/cycle), as determined by ellipsometry. To enhance the adhesion between Sb_2Se_3 and organic layers, UV treatment was performed on Sb_2Se_3/AL for 1 min before use. UV-treated samples were dipped into the precursor solution for 15 min followed by DI-rinsing and N_2 blowing. Subsequently, the samples were annealed on a hot plate in air at 80 °C for 15 min.

2.3. Fabrication of Sb_2Se_3 photocathodes with or without organic layer treatment

After the interface modification with the organic layers, the devices were immediately moved into the ALD chamber for additional TiO_2 deposition. For the reference photocathode without organic layer treatment, TiO_2 was directly deposited onto the as-prepared Sb_2Se_3 films. Using the same recipe as the previous AL deposition, 600 cycles were repeated allowing ~ 40 nm of TiO_2 (*c.f.*, here, only 30 cycles (~ 2 nm) were repeated to make the samples for the c-AFM analysis), followed by the sputtering Pt co-catalyst using an Auto Sputter Coater (Ted Pella, Redding, CA, USA) under an applied current of 10 mA for 120 s. For the stability test, a thin C_{60} layer was deposited prior to the Pt sputtering as described in our previous report [28]. Finally, a copper wire and silver paste were employed to form a contact with the electrode, and unnecessary parts of the electrode and the wiring parts were covered with an epoxy resin (HYSOL 9642, Henkel, Düsseldorf, Germany). For reproducibility test, each Sb_2Se_3 photocathde device was fabricated four times with the identical configuration. *2.4. PEC performance evaluation of Sb_2Se_3 photocathodes*

The LSV and chronoamperometry measurements of the Sb_2Se_3 photocathodes were performed in a typical three-electrode configuration with a Ag/AgCl/KCl (saturated) reference electrode and a coiled Pt wire as the counter electrode, using a potentiostat (1287A, Solartron, UK). All photocathodes, *i.e.*, working electrodes, and the reference/counter electrodes were immersed in an H_2SO_4 solution (pH 1), and the light source was simulated 1-sun illumination (AM 1.5 G, Newport Corporation) for all measurements. For calibration, a monocrystalline Si standard reference cell (Newport Corporation) was located at the same position of the sample for PEC measurement. The scan rate for the LSV measurement was 5 mV s^{-1}, while the applied potentials were recorded against the RHE to allow comparison with previously reported results, employing the relationship $E_{RHE} = E_{Ag/AgCl} + 0.059\ pH + 0.197$.

2.5. Characterizations of Sb_2Se_3 photocathodes

The surface and cross-sectional morphology of Sb_2Se_3 photocathodes were analyzed *via* field-emission scanning electron microscope (FE-SEM, JSM-7001 F, JEOL Ltd, Tokyo, Japan). The non-contact mode Kelvin probe force microscopy (KPFM, NX-10, Park Systems) measurements were performed using a gold-coated silicon cantilever to obtain the topography and corresponding surface potentials of Sb_2Se_3 samples. For quantitative analysis of the local work functions, Gwyddion software was employed to measure the local CPD values of Sb_2Se_3 grains. The c- AFM (SPA 400, Seiko Instruments, Inc., Chiba, Japan) analysis was performed using a rhodium-coated cantilever (SI-DF3-R) to obtain topographic images and current maps for the different Sb_2Se_3 devices. A silver paste was used to make a contact with conductive holder disk and the on-glass samples, while a bias of 1.0 V was applied between the electrode and the c-AFM probe tip under a solar simulator light of 0.2- sun to systematically describe the Sb_2Se_3/TiO_2 buried junction at the onset potential region. EIS measurements were directly performed after the LSV measurements in the same configuration using a potentiostat (1287A, Solartron, UK) combined with a frequency analyzer (1260, Solartron, UK). The polarization resistances were analyzed as a function of an applied cathodic potential with respect to the onset potential of each photocathode, in the

frequency range of 300 kHz to 0.01 Hz, at an AC amplitude of 10 mV, and under 1-sun illumination.

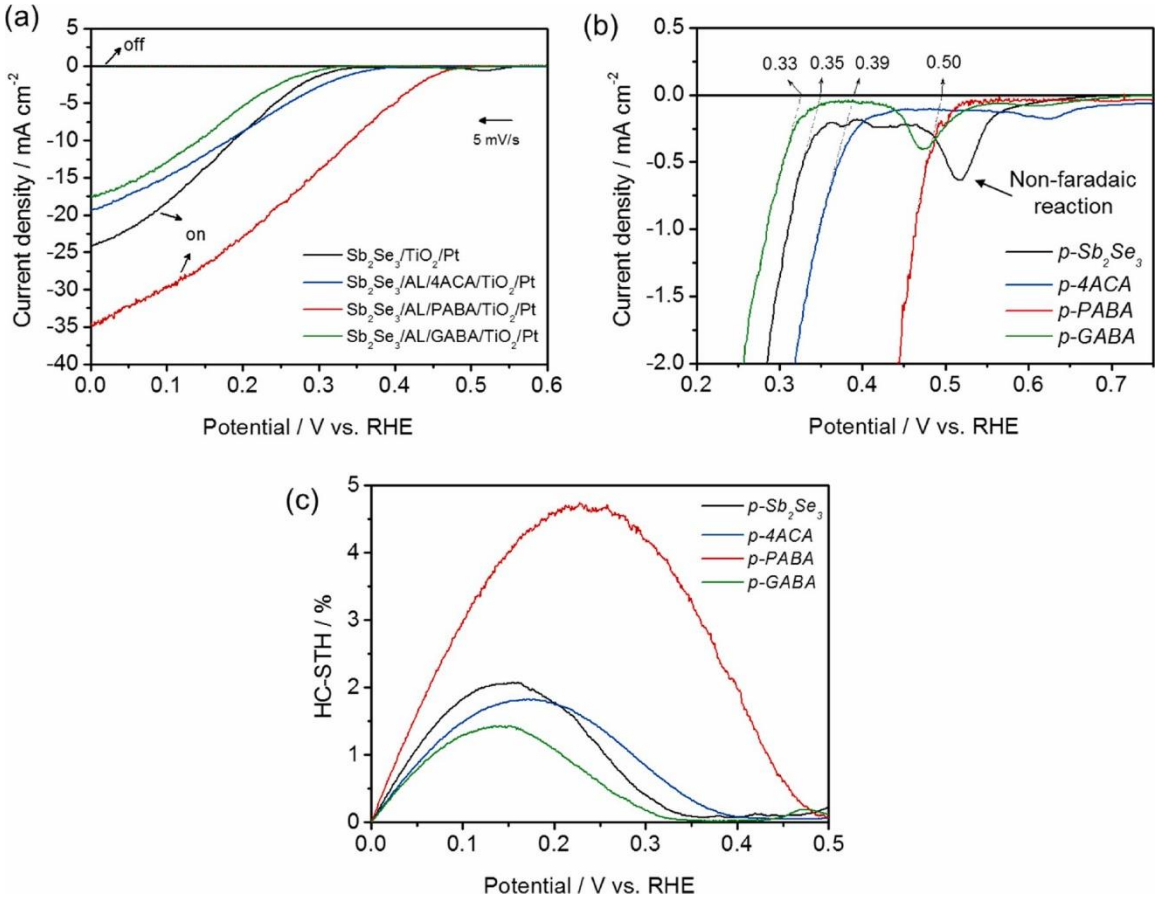

Fig. 2. (a) The J_{ph} variations of the four Sb_2Se_3 photocathodes. (b) Enlarged view of the onset potential region of (a). Each LSV curve was extrapolated within the rapidly increasing region to precisely determine the onset potential. (c) HC-STH conversion efficiency.

It was also performed at a fixed frequency at 100 Hz with the light chopping under − 0.1 V of the applied potential from each onset potential. IMPS measurements were performed employing an electrochemical workstation (Zennium, Zahner, Germany) combined with a potentiostat (PP211, Zahner, Germany) while the modulation intensity of light was 10 %. The frequency of the modulation was swept from 10 kHz down to 0.1 Hz

3. Results and discussion

3.1. Surface restoration of the polycrystalline Sb_2Se_3 films

Anchoring layer and organic layer were inserted into the boundary between FTO/Au/Sb_2Se_3 and TiO_2/Pt to fabricate interface-modified photocathode (Fig. 1a). Photocathode with a configuration of FTO/Au/Sb_2Se_3/TiO_2/Pt was employed as a reference device without interface modification. Three types of amino acids, *i.e.*, a benzene ring- containing PABA, a cyclohexane ring-containing 4-aminocyclohexanecarboxylic acid (denoted as 4ACA) and an alkyl chain-containing γ-aminobutyric acid (denoted as GABA), were selected as candidate organic layers (Fig. 1b). Prior to the organic layer coating, an anchoring layer (denoted as AL, *i.e.*, ~ 0.6 nm-thick amorphous TiO_2) was deposited to generate –OH bonds on Sb_2Se_3 surface which can strongly interact with the carboxyl group of amino acids to enhance the adhesion (see Experimental section for details). For convenience, the reference photocathode (*i.e.*, FTO/Au/Sb_2Se_3/TiO_2/Pt) was denoted as *p-Sb_2Se_3*, whereas three interface modified photocathodes (*i.e.*, FTO/Au/Sb_2Se_3/AL/organic layer/TiO_2/Pt) were denoted as *p-PABA*, *p-4ACA*, and *p- GABA* according to organic layer type. The morphologies of as-prepared Sb_2Se_3 film and after PABA treatment and TiO_2 protection layer deposition were observed by scanning electron microscopy (SEM) (Fig. S1, It is noted that the treatment of either 4ACA or GABA gave a rise to nearly identical microstructures as compared with PABA). Similar surface and cross-sectional microstructures regardless of sample types were evident, indicating that the introduction of the AL/organic layer did not alter the morphology of photocathodes. It should be noted that the thickness of overlayer from Sb_2Se_3/TiO_2 and Sb_2Se_3/AL/PABA/TiO_2 structure was 40.3 nm and 40.6 nm, respectively, implying that the thickness of PABA layer is nearly negligible, which is in a good agreement with the ellipsometry result (Fig. S2). In addition, the X-ray diffraction (XRD) patterns exhibited similar peak positions and shapes regardless of PABA treatment and TiO_2 layer deposition, suggesting that the photocathodes are fabricated without crystallinity variation of Sb_2Se_3 (Fig. S3).

3.2. Photoelectrochemical performances

Fig. 2a shows the J_{ph} variations for the four different Sb_2Se_3 based photocathodes, measured *via* linear sweep voltammetry (LSV) under 1- sun illumination. The J_{ph} of *p-Sb_2Se_3* at 0 V_{RHE} increased from 24 to 35 mA cm^{-2} upon the insertion of PABA, whereas *p-4ACA* and *p-GABA* treatments revealed the J_{ph} of 20 and 18 mA cm^{-2}, respectively. The reproducibility of photocathode performance was confirmed by measuring separately fabricated multiple devices (Fig. S4). While the onset potentials are typically defined as the potential at which the steep J_{ph} curve begins, some literatures defined it as the potential where cathodic J_{ph} is firstly observed or shows 0.03 – 0.05 mA cm^{-2} [29]. We extrapolated the LSV curves at rapidly increasing region to precisely determine when the J_{ph} is mainly contributed to HER (Fig. 2b). With a simple PABA treatment, the onset potential of *p-Sb_2Se_3* positively shifted from 0.35 V_{RHE} to 0.5 V_{RHE} without any J_{ph} losses, thereby high maximum half-cell solar-to-hydrogen (HC-STH) conversion efficiency of 4.7 % was calculated (Fig. 2c), according to the equation HC-STH = $J_{ph} \times (E_{RHE} - E_{H+/H2})/P_{SUN} \times 100$ %, where E_{RHE} is the potential of the working electrode against the electrolyte solution with respect to the RHE, $E_{H+/H2}$ is 0 V_{RHE}, and P_{SUN} is 100 mW cm^{-2} [2]. This is the highest value of Sb_2Se_3 based photocathodes reported so far. It should be noted here that HC-STH is a convenient diagnostic efficiency for photoelectrodes with a three-electrode configuration, assuming 100 % of the Faradaic efficiency and negligible overpotential of the counter reaction (OER).

While the *p-4ACA* exhibited the onset potential of 0.39 V_{RHE}, but the fill factor and HC-STH were lower than those of *p-Sb_2Se_3*. All PEC performance factors of *p-GABA*, including the onset potential, J_{ph}, fill factor and HC-STH, were lower than the *p-Sb_2Se_3* counterparts. In our previous study [7], the insertion of an *n*-type CdS layer between Sb_2Se_3 and TiO_2 (*i.e.*, Sb_2Se_3/CdS/TiO_2/Pt photocathodes) also shifted the onset potential up to 0.5 V_{RHE}. However, the HC-STH (3.4 %) and J_{ph} (< 20 mA cm^{-2} at 0 V_{RHE}) of the Sb_2Se_3/CdS/TiO_2/Pt photocathodes were lower than *p-PABA* despite the toxic nature and the relatively complicated deposition of CdS. On the other hand, *p-PABA* exhibited a very steep J_{ph} increase starting from the onset potential showing the high HC-STH values, despite its simple deposition method, non-toxicity and low material usage, therefore it can be considered as an easy and promising strategy for enhancing the performance of photoelectrodes.

It should be noted that the *p-Sb_2Se_3* exhibited a temporal rise in reduction current (black colored curve) at ~ 0.55 V_{RHE}, followed by an abruptly increased current at 0.35 V_{RHE} (Fig. 2b). Interestingly, the temporal current disappeared when the LSV scan was repeated, while the onset potential and HER current remained almost identical (Fig. S5). We presume that this pre-reduction current peak contributes to the non- faradaic reaction occurred at the Sb_2Se_3/TiO_2 interface (*e.g.*, the reduction of interface states) and the disappearance of the pre-reduction peak after the PABA treatment is relevant to the enhanced V_{ph}. It should be noted that the contribution of other possible non-faradaic reactions such as adsorption or desorption of electrolyte ions at the surface of photocathodes should be nearly similar among all photocathodes because they involve identical surface structures of TiO_2/Pt/electrolyte (H_2SO_4). Interface modification with cyclohexane ring-containing 4ACA reduced area of pre-reduction current peak (blue), while the pre- reduction current became almost negligible when treated with benzene ring-containing PABA (red). By contrast, the chain-containing GABA still produced the current peak with a significant area (green). All aminobenzoic acids regardless of the orientation between amino and carboxyl group effectively prevented the non-faradaic reaction, whereas those with the absence of either amino or carboxyl group still exhibited the current peak even though they were conjugated molecules (Fig. S6). Since the area of pre-reduction peak is proportional to the amount of photoelectrons consumed for the non-faradaic reaction, it can be understood that ring-containing amino acids more effectively prevent the formation of interface state than those composed of alkyl chains. Although PABA and GABA have similar carbon (C) chain lengths and molecular sizes, PABA has lower steric hindrance compared with GABA owing to the π-π conjugated benzene ring in the molecule, which allows ordered lamellar packing and compact π–π stacking on the surface [25, 26,30]. It is speculated that the compact and highly ordered benzene rings could enable the effective surface restoration of the Sb_2Se_3 thin films as well as the rapid charge transfer from the Sb_2Se_3 to TiO_2, and thus the high J_{ph} and V_{ph}. In contrast, the stronger steric hindrance caused by the rotational $C(sp^3)$-$C(sp^3)$ bonds in GABA molecules could result in the non-uniform and less covered molecular layer. Moreover, the poor conductivity of the GABA layer can further cause a detrimental effect on the electron transfer from Sb_2Se_3 to TiO_2, which can lead to the poor performance of *p-GABA* [31,32]. The cyclohexane of 4ACA molecule is known to exist as either boat or chair structure having rotational bonds [33], thus the surface coverage of 4ACA on Sb_2Se_3 should be lower than PABA with benzene ring. Hereafter, for further analyses, we mainly considered PABA and 4ACA to demonstrate the influence of organic layer treatment on the PEC performance variations.

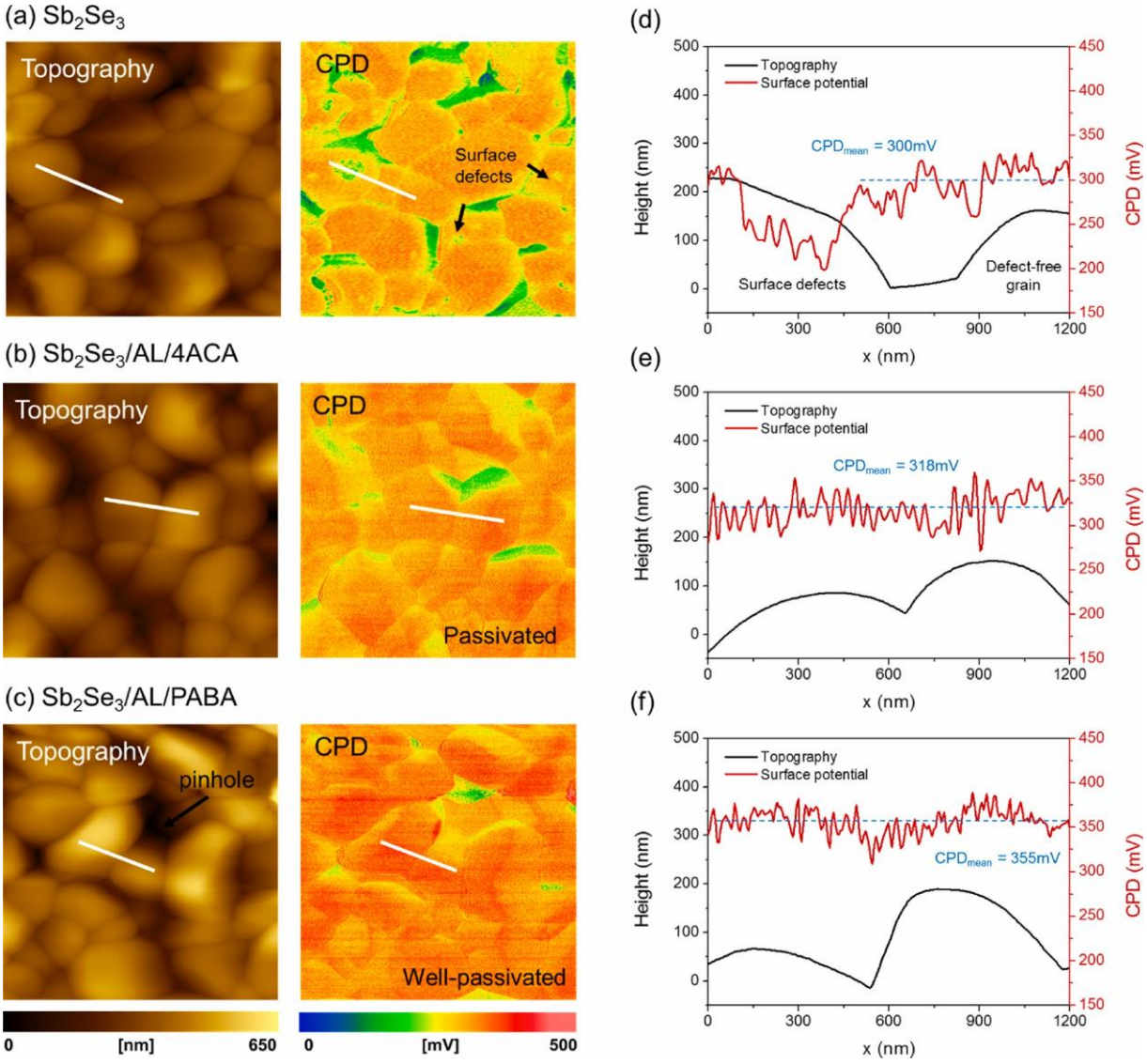

Fig. 3. (a) KPFM surface electronic structure analysis of the Sb_2Se_3 with and without the organic layer treatment. Topography and the corresponding CPD maps of the (a) Sb_2Se_3, (b) Sb_2Se_3/AL/PABA, and (c) Sb_2Se_3/AL/4ACA; (d–f) Line profiling of the topography and CPD for a representative Sb_2Se_3 grain from each sample.

3.3. Surface analysis of Sb_2Se_3 films

To understand the surface electronic structures of Sb_2Se_3 with or without organic layers, we separately prepared three different samples of Sb_2Se_3 films depending upon different surface treatment (*i.e.*, Sb_2Se_3, Sb_2Se_3/AL/PABA and Sb_2Se_3/AL/4ACA) followed by Kelvin probe force microscopy (KPFM) analysis, which allowed us to investigate the topography as well as the contact potential difference (CPD) within a local region (Fig. 3). Although the topology of Sb_2Se_3 is independent to the organic layer treatment as observed by SEM analysis, relatively low CPD spots are observed not only at the grain boundaries but also within the grain of Sb_2Se_3 possibly due to surface defects, which might include partial oxidation or dangling bonds of surface Sb_2Se_3 (arrows in Fig. 3a). The CPD clearly becomes uniform over Sb_2Se_3 grains and grain boundaries in the presence of the organic layer, indicating that surface defects are well-passivated after the modification (Fig. 3b and c). Moreover, even a large pinhole is observed from the topological image of Sb_2Se_3/AL/PABA, the corresponding CPD is not as low as the counterpart of Sb_2Se_3. These observations indicate that the surface treatment with the ring-containing organic molecules effectively flattens the fluctuation of the surface potential due to pin-holes and surface defects, which can potentially cause performance degradation. The surface potential fluctuation along with the pre-reductive current can lead us to conclude that the surface defects (presumably in oxidized states) on Sb_2Se_3 thin films are reduced during the device operation by taking the photoelectrons and creating interface states which are detrimental for the device performance. Thus, it is reasonably presumed that the surface of the Sb_2Se_3 thin films are restored by the organic molecules and thereby the formation of the detrimental interface states is suppressed that leads to higher performance, particularly in V_{ph}.

Apart from the passivation of the surface states, another possible origin of the V_{ph} enhancement is the dipole effect induced by inserting a highly polarizable layer that increases the band bending as reported by Wick-Joliat et al. [17] Although it is difficult to directly measure the band bending in a *p-n* junction, the degree of band bending can be estimated by the work function (Φ) difference between the two semiconductors. In the case of absolute values of Φ measured in KPFM, it is generally considered that the reliability is high only in a ultra high vacuum condition, but when proper calibration of the tip is performed, relative comparison between samples even at ambient pressure can be performed with high reliability. We employed a freshly cleaved highly oriented pyrolytic graphite (HOPG, Φ_{HOPG} =4.48 eV, confirmed by ultraviolet photoelectron spectroscopy) as a reference sample and the tip was calibrated *via* equation $\Phi_{Tip} = \Phi_{HOPG} + eU_{HOPG/CPD}$, where $U_{HOPG/CPD}$ is the surface potential measured by KPFM. Topography and potential line profiling for the Sb_2Se_3 film

Fig. 4. c-AFM analyses performed on the (a) Sb_2Se_3/TiO_2, (b) Sb_2Se_3/AL/4ACA/TiO_2, and (c) Sb_2Se_3/AL/PABA/TiO_2. Each buried junction of the photocathodes under the onset potential region was systematically analyzed after depositing a thin (≈2 nm) TiO_2 layer by applying a relatively small bias (1 V) under illumination (0.2 sun). Images of the topography (left) and the corresponding photocurrent map (right) as well as their line profiles (bottom) for a single Sb_2Se_3 grain of each sample are shown.

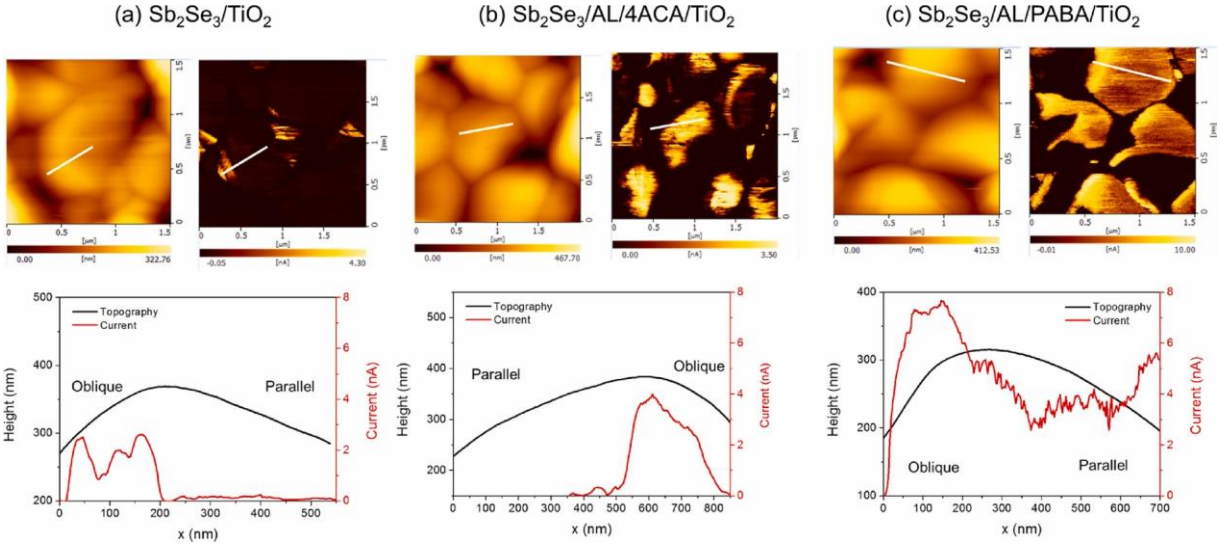

suggested that the CPD values near surface defects are ~ 100 mV smaller than other regions of grain (Fig. 3d). After the organic layer treatment, mean CPD values are 318 and 355 mV for Sb_2Se_3/AL/4ACA (Fig. 3e) and Sb_2Se_3/AL/PABA (Fig. 3f), respectively, which are both slightly larger than that of the bare Sb_2Se_3 (300 mV). The Φ values, calculated by the equation $\Phi_{Sb2Se3} = \Phi_{Tip} - eU_{Sb2Se3/CPD}$ [34], was 4.51, 4.49, and 4.46 eV for Sb_2Se_3, Sb_2Se_3/AL/4ACA, and Sb_2Se_3/AL/PABA, respectively. Fig. S7 shows the relative positions of calculated Φ values with respect to the E_F of semiconductor. The slight Φ variation and the resulting difference in the estimated band bending depending on the surface treatment indicates the possible surface dipole effect, but the contribution to the band bending at Sb_2Se_3/TiO_2 interface is almost negligible. Thus, it is reasonable to conclude that the significantly enhanced V_{ph} in *p-PABA* results from the passivation of the surface defects, rather than the dipole effect. Considering the small CPD near the surface defects, the Fermi energy pinning upon light illumination due to the surface defects seems to be the main cause of the small V_{ph} in *p-*Sb_2Se_3, as shown in Fig. S8.

To further understand the photoelectron behaviour at the buried junction, we additionally coated a thin TiO_2 layer (~ 2 nm) onto three representative samples (*i.e.*, Sb_2Se_3/TiO_2, Sb_2Se_3/AL/PABA/TiO_2, and Sb_2Se_3/AL/4ACA/TiO_2), followed by a conductive AFM (c-AFM) measurement under illumination which can detect local variations of surface photocurrent. Differently from the non-contact mode of KPFM, the c- AFM requires a tip contacting the surface of samples, so that noise-like behaviour due to scratch of organic molecules was likely observed without TiO_2 overlayer. Since the tip-contacted surface can be considered as the Sb_2Se_3/TiO_2 buried junction in photocathode, the onset potential region (*i.e.*, where a steep increase in photocurrent begins) was systematically analyzed by applying a relatively small bias (1 V). As shown in Fig. 4a, comparing the photocurrent map with the corresponding topographic image revealed that the photocurrents were unevenly detected over the grains. A line profile over a single grain clearly showed an asymmetric photocurrent distribution. This result originates from the anisotropic property of Sb_2Se_3 in which the photogenerated charges are readily transported particularly along the direction of aligned $[Sb_4Se_6]_n$ ribbons [35–38]. It can be assumed that the grains become conductive if the $[Sb_4Se_6]_n$ ribbons are oblique with respect to the grain surface (*i.e.*, oblique region, ~ 2 nA), whereas the photocurrent is unobservable when the ribbons are parallel to the grain surface (*i.e.*, parallel region, 0 nA). The aligned structure of $[Sb_4Se_6]_n$ ribbons at two different regions are schematically shown in Fig. S9. In the case of Sb_2Se_3/AL/4ACA/TiO_2, the photocurrent of the parallel region still remained nearly zero, while the PABA-treated sample revealed highly amplified photocurrent levels in both the oblique (5–8 nA) and parallel (3–5 nA) regions (Fig. 4b and c). This is presumably originated from the π-electron delocalized conjugated orbitals of PABA molecules. Conjugated molecules bi-functionally enable the efficient collection of electrons from its surrounding followed by a rapid transfer to another neighbouring material, acting as an excellent electron donor–acceptor molecular system. To take advantages of these characteristics, conjugated electron donor–acceptor molecules have received increasing attention as an interface candidate for improving the charge transport efficiency between the absorbing layer and electrode in optoelectronic applications [21]. We speculated that under very low applied potential, only the photoelectrons generated near the Sb_2Se_3/AL/PABA interface can be easily redistributed in the conjugated orbitals of PABA followed by a rapid transfer to the TiO_2 layer. The highly amplified photocurrent in Sb_2Se_3/AL/PABA/TiO_2 serve a role as supportive evidence to explain the improved J_{ph} in *p-PABA*. *3.4. Photoelectrochemical characterizations*

To elucidate the influence of PABA treatment for the PEC performance, we further investigate the charge transport behaviour for the photocathode devices of *p-*Sb_2Se_3 and *p-PABA*. The electrochemical impedance spectroscopy (EIS) allows us to understand the charge transport and transfer kinetics by analyzing the polarization arc as a function of the frequency [39,40]. After a single scan of LSV for *p-*Sb_2Se_3 and *p-PABA*, we performed EIS measurements in the frequency range of 300 kHz to 0.01 Hz under 1-sun illumination at the onset potentials, and subsequently under negatively applied potentials of 0.02, 0.05, and 0.10 V. As shown in Fig. 5a, the Nyquist plot of the *p-*Sb_2Se_3 at the onset potential (0.35 V_{RHE}, black) exhibited two sub-arcs, consisting of the small one in a high frequency region and the large one in a low frequency region. With increasing applied potentials, the small arc remained almost identical, whereas the large one clearly became smaller and separated into two sub-arcs again, which was further confirmed by the corresponding Bode plot (Fig. 5b). A large peak observed in a range

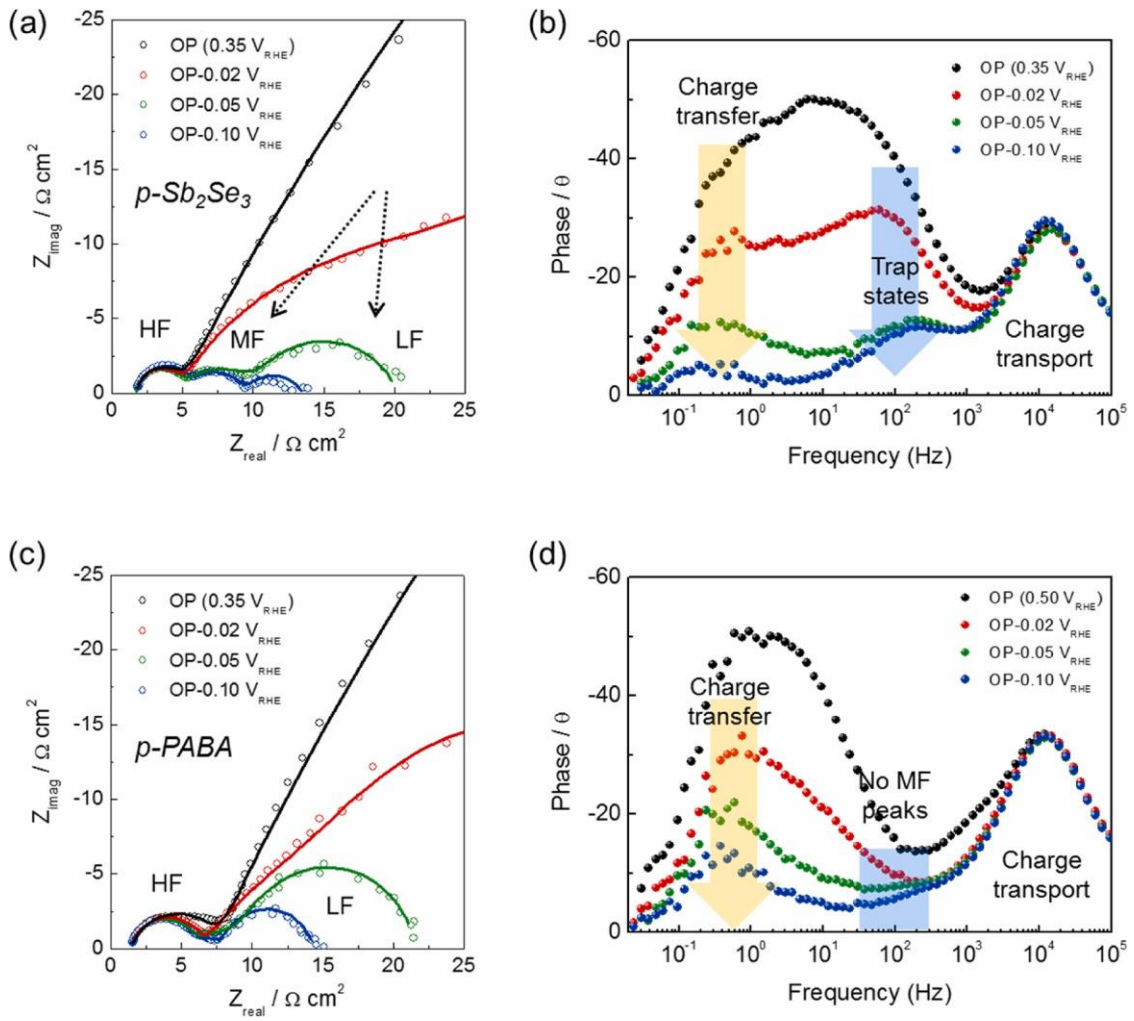

Fig. 5. (a) Nyquist plots and the corresponding Bode plots for the (a) and (b) *p-Sb_2Se_3* and (c) and (d) *p-PABA*. After a single LSV scan of the *p-Sb_2Se_3* and *p-PABA*, the EIS measurement was performed in the frequency range of 300 kHz to 0.01 Hz under 1 sun illumination at the onset potential, and then under applied potentials of 0.02, 0.05, and 0.10 V. 'OP' stands for the onset potential and 'OP – 0.10' corresponds to 0.25 and 0.40 V_{RHE}. In the Nyquist plots, scatter points stand for the original experimental data, whereas solid lines represent fitted curves based on the equivalent circuit as shown in Fig. S10a.

of 1 kHz – 0.1 Hz (black) decreased with more applied potentials, while the peak was simultaneously separated into two sub-peaks with characteristic frequencies of ~ 100 Hz and ~ 0.3 Hz. A peak at ~ 10 kHz did not show significant variation. On the other hand, in Nyquist plot of *p-PABA*, the large low frequency arc continuously decreased without noticeable separation under more applied potentials (Fig. 5c), while the peaks at ~100 Hz in Bode plot are almost negligible regardless of the applied potentials (Fig. 5d).

To precisely fit the obtained EIS spectra, we employed an equivalent circuit model consisting of three serially connected resistor–capacitor

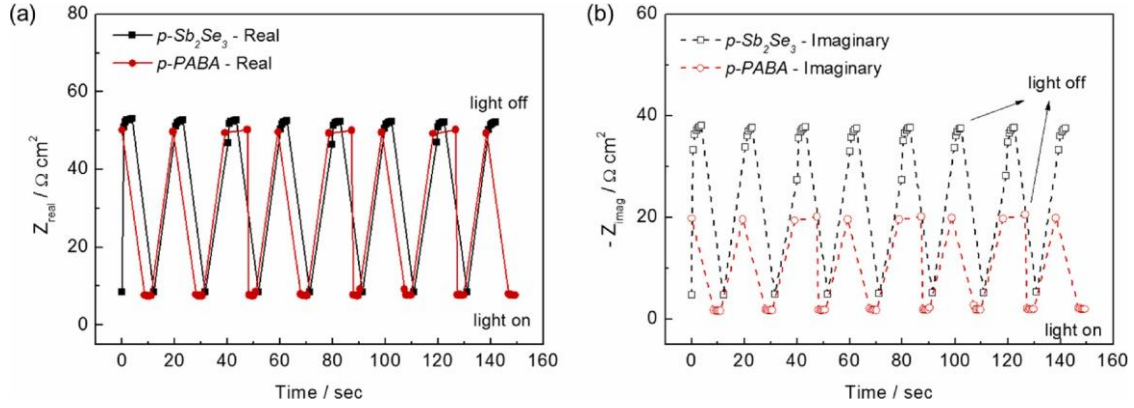

Fig. 6. (a) Real (Z_{real}) and (b) Imaginary (Z_{imag}) parts of the complex impedance values of the *p-Sb_2Se_3* and *p-PABA*. The EIS was performed at a fixed frequency of 100 Hz with light chopping and an applied potential of -0.1 V from each onset potential.

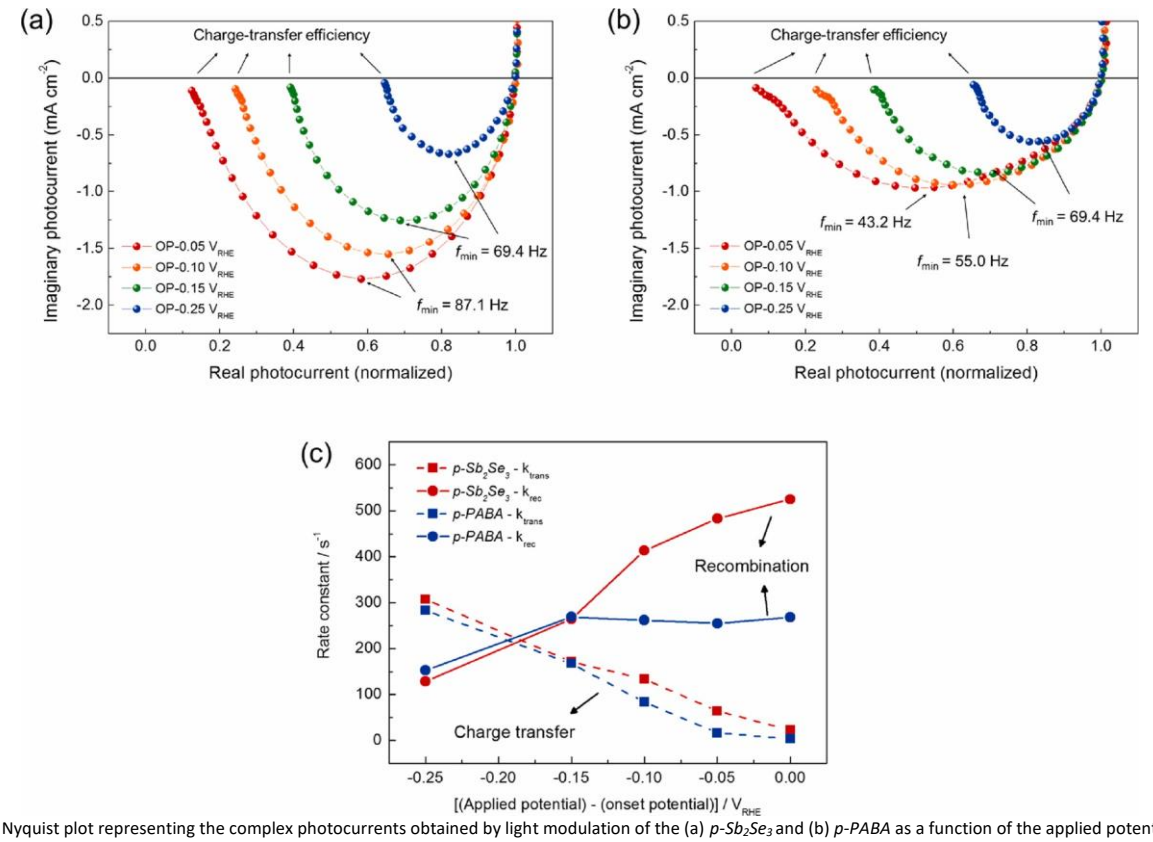

Fig. 7. (a) IMPS Nyquist plot representing the complex photocurrents obtained by light modulation of the (a) *p-Sb_2Se_3* and (b) *p-PABA* as a function of the applied potential with respect to each onset potential. f_{min} represents the frequency at the bottom of the semicircle. (c) k_{trans} and k_{rec} calculated from each semicircle of the *p-Sb_2Se_3* and *p-PABA*.

blocks with a resistance (R) and a constant phase element (CPE) at three different frequency ranges (Fig. S10a). For convenience, the three deconvoluted semicircles were classified into high-frequency resistance (R_{HF}) with capacitance (CPE_{HF}), middle-frequency resistance (R_{MF}) with capacitance (CPE_{MF}), and low-frequency resistance (R_{LF}) with capacitance (CPE_{LF}), representing the characteristic frequencies of 10 kHz, 100 Hz, and 0.3 Hz, respectively. The fitted results for both photocathodes are summarized in Table S1. It has been suggested that the HF arc is influenced by the charge transport resistance (R_{HF}) within the electrode with the capacitance of the bulk semiconductor (CPE_{HF}); the MF arc represents the resistance (R_{MF}) with the capacitance (CPE_{MF}) of charge trapping at the trap states within the band gap; the LF arc reflects the resistance of electrochemical charge-transfer reactions (R_{LF}, *e.g.*, HER) with the double layer capacitance (CPE_{LF}) [28,41–43]. The obtained R_{MF} and R_{LF} values for both photocathodes as a function of applied potential are shown in Fig. S10b. For *p-Sb_2Se_3*, after the HER begins at the onset potential, therefore, an applied potential is mainly used for not only enhancing the charge transfer kinetics but also overcoming the trap state-derived losses. Because the electrode/electrolyte interface is practically identical for both *p-Sb_2Se_3* and *p-PABA*, the charge transfer variations as a function of applied potential are similarly observed only in LF region. For *p-PABA*, however, since the characteristic frequency in Bode plots reflects the characteristic time for the underlying photo-physical (or electrochemical) phenomena, the negligible R_{MF}, particularly at near onset potential, implies that the treatment is capable of eliminating one resistive-pathway of electrons. The R_{MF} is presumably associated with the traps generated at the Sb_2Se_3/TiO_2 interface, which is in agreement with the surface defects restoration observed in KPFM analysis and the negligible pre-reductive current peak from LSV measurement. Our previous study demonstrated that the MF peak at ~ 300 Hz also appears when photogenerated electrons are trapped in the surface trap states of TiO_2 [28].

To further study the role of the interface states, we additionally performed EIS at a fixed frequency of 100 Hz (*i.e.*, MF region) with light chopping under − 0.1 V of applied potential from each onset potential (Fig. 6). Note that the real part value of complex impedance (Z_{real}) corresponds to the resistance whereas the imaginary part (Z_{imag}) reflects the information of the capacitive reactance when the values are negative. Because the J_{ph} was almost the same when the applied potential from the photocurrent onset was identically − 0.1 V (*i.e.*, − 4.5 mA cm^{-2} at 0.25 V_{RHE} for *p-Sb_2Se_3* and − 4.8 mA cm^{-2} at 0.4 V_{RHE} for *p-PABA*, Fig. 1c), the Z_{real} and Z_{imag} values under light-on condition were also similar for two photocathodes. However, the Z_{imag} value, which increased rapidly when the light was turned off (Fig. 6b), was inversely proportional to the interface capacitance which can be physically described as the accumulation of photoelectrons at the interface. The amount of accumulated photoelectrons at the interface of *p-Sb_2Se_3* was approximately halved in comparison with the *p-PABA* possibly due to the interface states-induced rapid recombination. On the other hand, instead of the MF peaks, a small shoulder HF peak in a frequency range of 10 kHz – 1 kHz was solely observed when EIS was performed at the onset potential of *p-PABA*, implying slightly altered charge transport pathway particularly at the onset potential.

To better understand how PABA treatment would affect the photoelectron transport properties in photocathodes, we performed the IMPS technique which becomes increasingly popular for understanding the charge carrier dynamics and its influence on PEC performance [44–47]. Differently from the EIS that measures the current output by applying a small voltage perturbation, the IMPS determines the extracted current as a function of the perturbation frequency of the light illumination while it is more easy to extract rate constants for charge transfer and recombination processes. Fig. 7a,b show Nyquist plots representing the complex photocurrent of *p-Sb_2Se_3* and *p-PABA*, respectively, obtained by light modulation as a function of applied potential with respect to each onset

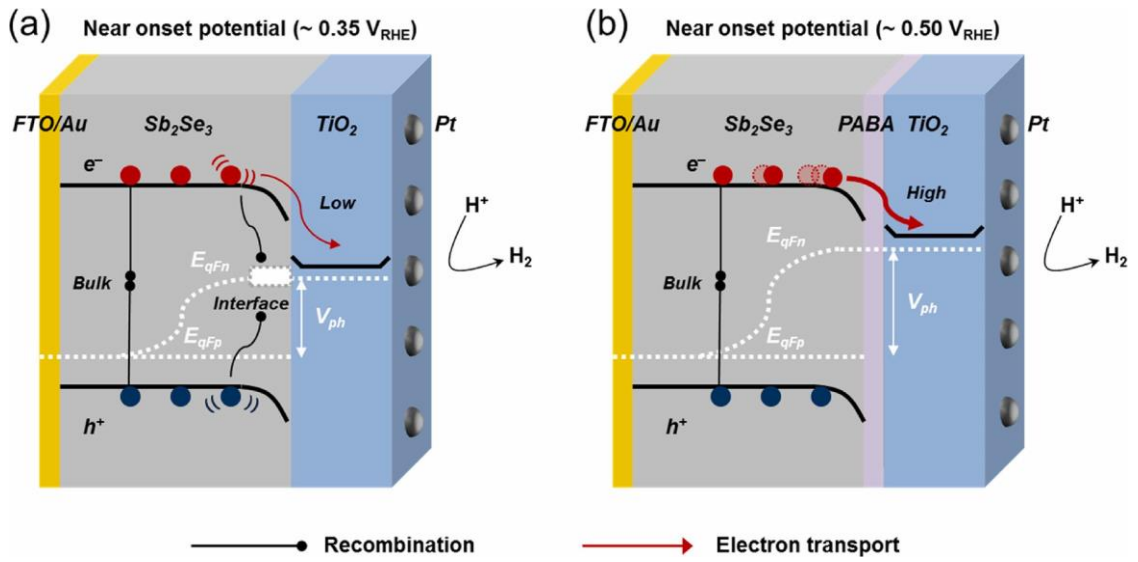

Scheme 1. Schematic illustration of (a) $Sb_2Se_3/TiO_2/Pt$ and (b) $Sb_2Se_3/AL/PABA/TiO_2/Pt$ photocathodes describing the photoelectron behaviour at near the onset potential region.

potential. When the real photocurrent is normalized to the high-frequency intercept, the low-frequency intercept indicates the charge-transfer efficiency, defined as $k_{trans}/(k_{trans} + k_{rec})$, where k_{trans} and k_{rec} are the surface charge transfer and recombination rate constants, respectively. The combined rate of charge transfer and recombination can be calculated from the relation $k_{trans} + k_{rec} = 2\pi f_{min}$, where f_{min} is the frequency at the bottom of the semicircle observed in the IMPS plots [44]. By combining the charge-transfer efficiency and f_{min}, both k_{trans} and k_{rec} can be calculated (The values are shown in Tables S2 and S3). In *p-Sb₂Se₃*, there was only one distinct semicircle regardless of applied potentials, suggesting only one electron transport mode with a mean transit time, *i.e.*, $\tau_t = 1/(k_{trans} + k_{rec})$, whereas *p-PABA* exhibited two semicircle features only at the onset potential (Fig. S11). Because the obtained τ_t values for the photoelectron transport were within a range of 1–4 ms except for the fisrt semicircle measured at the onset potential of *p-PABA* which was one order lower (*i.e.*, τ_t =0.37 ms), we considered the second semicircle for calculating rate constants. The first semicircle of *p-PABA* under the onset potential may represents another reaction with different characteristic transit time, such as charge redistribution in conjugated PABA molecules. It seems that this arc is only observable when overall photocurrent is not significant. The calculated k_{trans} and k_{rec} as a function of the applied potential are presented in Fig. 7c. The k_{trans} for both *p-Sb₂Se₃* and *p-PABA* similarly increase with an increase in the applied cathodic potential with respect to the onset potential. In contrast, the k_{rec} for *p-PABA* is significantly lower than that of *p-Sb₂Se₃* particularly near the onset potential region. This result suggests that the PABA treatment at Sb_2Se_3/TiO_2 interface well-prevent the charge recombination process, which typically occurs at the detrimental interface state. Therefore, it is clear that the surface restoration of Sb_2Se_3 using PABA molecules effectively passivate the surface defects, in agreement with KPFM result and the negligible pre-reductive current peak from LSV measurement, leading to high onset potential and photocurrent of photocathodes.

3.5. Discussion

The significance of surface restoration with PABA molecule as well as the photoelectron behavior from a single Sb_2Se_3 grain near the onset potential region are schematically illustrated in Scheme 1. At near the onset potential region with low applied potential, because the polycrystalline Sb_2Se_3 films inevitably have surface defects, the photoelectron transport is interrupted by an interface recombination, lowering the overall photocurrent, while no photocurrent is observed in the parallel region of the grain (Scheme 1a and Fig. S12a). Surface restoration of these Sb_2Se_3 not only produces high V_{ph} in Sb_2Se_3/TiO_2 buried junction without fermi level pinning, but also enables a rapid photoelectron transport from Sb_2Se_3 to TiO_2 layer through conjugated PABA molecule, maximizing the photocurrent in both parallel and oblique regions (Scheme 1b and Fig. S12b). Moreover, if the inserted organic molecules having fully saturated bonds such as 4ACA are electrically insulating, an additional resistance for electron flow can be posed even when high V_{ph}. The interface states in Sb_2Se_3/TiO_2 reduce the number of electrons

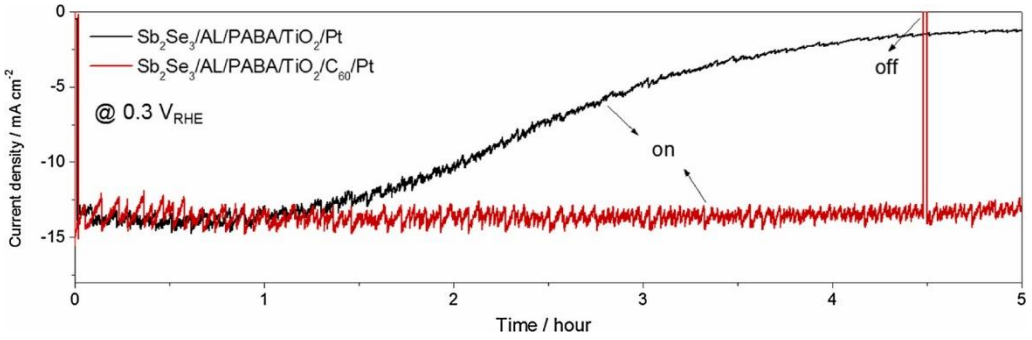

Fig. 8. Photocurrent stability tests of the *p-PABA* with and without C_{60} modification at the TiO_2/Pt interface. The chronoamperometry measurement was performed at 0.3 V_{RHE} in pH 1 electrolyte under continuous illumination.

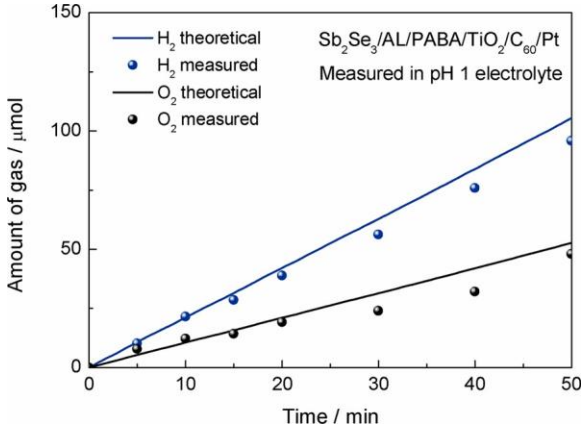

Fig. 9. Hydrogen and oxygen production as a function of the operating time during the stability testing of the Sb_2Se_3/AL/PABA/TiO_2/C_{60}/Pt device. The solid line represents the ideal curve calculated for 100 % Faradaic efficiency, whereas the circles indicate the experimentally detected gas production, which was quantified using gas chromatography.

crossing the buried junction, whereas the additional resistance in Sb_2Se_3/AL/4ACA/TiO_2 should be considered as a threshold phenomenon in which electrons can travel only when sufficient potential is applied to overcome the energy barrier. This is in an agreement with LSV result in which a small photocurrent is continuously observed prior to steep increase for *p-Sb_2Se_3*, whereas the photocurrent is almost negligible after the 4ACA treatment (Fig. 2b). Therefore, the conjugated characteristic of PABA which allows a rapid photoelectron transport at Sb_2Se_3/TiO_2 interface is critically imperative to achieve high J_{ph} and V_{ph} photocathodes.

3.6. Stability and hydrogen generation

The stable operation of the photocathode is of significant interest for its practical application in PEC devices [48]. The photocurrent stability of the *p-PABA* was tested in the argon-purged pH 1 electrolyte at 0.3 V_{RHE} under continuous illumination to evaluate the device stability under low applied potential region. Since PABA is known as stable molecule under solar irradiation and hardly decomposed unless it reacts with strong oxidant in aqueous solution [49], TiO_2-protection strategy, which physically separates the inner layer from the electrolyte, is an appropriate approach for achieving the stability. As shown in Fig. 8, our *p-PABA* revealed the two-step degradation of the photocurrent; a linearly decreasing region followed by an exponentially diminishing region after an initial short stable region of 1 h. In our previous study, we demonstrated that the accumulation of photoelectrons at the surface of TiO_2 protective layer induced the reductive dissolution gradually from the surface, which is responsible for the linear photocurrent degradation [28]. As the TiO_2 layer dissolves to disrupt the *p-n* junction, Sb_2Se_3 and PABA layer become also directly exposed to the electrolyte, possibly causing surface corrosion or decomposition, as expressed by an exponential degration of photocurrent. With fullerene (C_{60}) modification at TiO_2/Pt interface, the photoelectron could rapidly transfer out of the TiO_2 layer while suppressing the accumulation, thereby exhibiting stable operation over 5 h under the same electroylte at 0.3 V_{RHE}. During the stable operation of Sb_2Se_3/AL/PABA/TiO_2/C_{60}/Pt device, the amount of photoelectrochemically produced H_2 and O_2 gas were also quantified by gas chromatography analysis. The molar ratio of H_2 and O_2 was close to 2:1, corresponding to the theoretically calculated amount and showing a Faradaic efficiency within a range of 90–100 % (Fig. 9).

4. Conclusions

We introduced a simple interface modification strategy by which the onset potential and photocurrent of Sb_2Se_3 photocathode was maximized by restoring the Sb_2Se_3/TiO_2 interface with PABA molecules. The PABA-decorated Sb_2Se_3/AL/PABA/TiO_2/Pt photocathode exhibited a high onset potential of 0.5 V_{RHE}, photocurrent density of 35 mA cm^{-2} at 0 V_{RHE}, and HC-STH of 4.7 %, representing the highest performance of Sb_2Se_3 photocathode so far. It was demonstrated that ring-containing amino acids, both PABA and 4ACA, effectively passivated the surface defects of polycrystalline Sb_2Se_3 thin film. Without the treatment, the produced photovoltage at buried junction is low due to interface state- induced fermi level pinning, while those interface states act as recombination center, decreasing the photocurrent. By surface restoring of Sb_2Se_3 with PABA, the photoelectrons were efficiently extracted over whole grains of anisotropic Sb_2Se_3, whereas Sb_2Se_3 or 4ACA-treated Sb_2Se_3 showed only one-way photocurrent flow under low applied potential. We elucidated that a rapid charge transport through Sb_2Se_3/ TiO_2 interface is allowed in the presence of PABA by suppressing the interface state-derived recombination particularly near onset potential region. Our study clearly suggests a simple interface treatment strategy to maximize both the onset potential and photocurrent of polycrystalline thin film-based photocathodes for PEC water splitting.

Acknowledgments

This work was supported by the National Research Foundation (NRF) of Korea grant (No. 2012R1A3A2026417) and the Creative Materials Discovery Program (NRF-2018M3D1A1058793) funded by the Ministry of Science and ICT, and the UK's Engineering and Physical Sciences Research Council (EPSRC) grant EP/N010457/1. This work was also supported by the Technology Innovation Program - Alchemist Project (No. 20012315) funded by the Ministry of Trade, Industry & Energy (MOTIE, Korea).

Appendix A. Supplementary data

Supplementary material related to this article can be found, in the online version, at XXXXXXX.

References

[1] M. Gratzel, Alternative energy technologies, Nature 414 (2001) 338¨ –344, https:// doi.org/10.1038/35104599.

[2] T. Hisatomi, J. Kubota, K. Domen, Recent advances in semiconductors for photocatalytic and photoelectrochemical water splitting, Chem. Soc. Rev. 43 (2014) 7520–7535, https://doi.org/10.1039/c3cs60378d.

[3] K. Sivula, R. van de Krol, Semiconducting materials for photoelectrochemical energy conversion, Nat. Rev. Mater. 1 (2016) 15010, https://doi.org/10.1038/ natrevmats.2015.10.

[4] W. Yang, R.R. Prabhakar, J. Tan, S.D. Tilley, J. Moon, Strategies for enhancing the photocurrent, photovoltage, and stability of photoelectrodes for photoelectrochemical water splitting, Chem. Soc. Rev. 48 (2019) 4979–5015, https://doi.org/10.1039/C8CS00997J.

[5] Y. Dai, J. Yu, C. Cheng, P. Tan, M. Ni, Engineering the interfaces in water-splitting photoelectrodes – an overview of the technique development, J. Mater. Chem. A 8 (2020) 6984–7002, https://doi.org/10.1039/D0TA01670E.

[6] Y. Kuang, T. Yamada, K. Domen, Surface and interface engineering for photoelectrochemical water oxidation, Joule 1 (2017) 290–305, https://doi.org/ 10.1016/j.joule.2017.08.004.

[7] W. Yang, J.H. Kim, O.S. Hutter, L.J. Phillips, J. Tan, J. Park, H. Lee, J.D. Major, J. S. Lee, J. Moon, Benchmark performance of low-cost Sb2Se3 photocathodes for unassisted solar overall water splitting, Nat. Commun. 11 (2020) 861, https://doi. org/10.1038/s41467-020-14704-3.

[8] T. Wang, Y. Wei, X. Chang, C. Li, A. Li, S. Liu, J. Zhang, J. Gong, Homogeneous Cu2O p-n junction photocathodes for solar water splitting, Appl. Catal. B Environ. 226 (2018) 31–37, https://doi.org/10.1016/j.apcatb.2017.12.022.

[9] L. Pan, J.H. Kim, M.T. Mayer, M.-K. Son, A. Ummadisingu, J.S. Lee, A. Hagfeldt, J. Luo, M. Gratzel, Boosting the performance of Cu2O photocathodes for unassisted ¨ solar water splitting devices, Nat. Catal. 1 (2018) 412–420, https://doi.org/ 10.1038/s41929-018-0077-6.

[10] C. Li, T. Hisatomi, O. Watanabe, M. Nakabayashi, N. Shibata, K. Domen, J.- J. Delaunay, Positive onset potential and stability of Cu2O-based photocathodes in water splitting by atomic layer deposition of a Ga2O3 buffer layer, Energy Environ. Sci. 8 (2015) 1493–1500, https://doi.org/10.1039/C5EE00250H.

[11] M. Chen, Y. Liu, C. Li, A. Li, X. Chang, W. Liu, Y. Sun, T. Wang, J. Gong, Spatial control of cocatalysts and elimination of interfacial defects towards efficient and robust CIGS

photocathodes for solar water splitting, Energy Environ. Sci. 11 (2018) 2025–2034, https://doi.org/10.1039/C7EE03650G.
[12] Y. Fu, C.-L. Dong, W. Zhou, Y.-R. Lu, Y.-C. Huang, Y. Liu, P. Guo, L. Zhao, W.- C. Chou, S. Shen, A ternary nanostructured α-Fe2O3/Au/TiO2 photoanode with reconstructed interfaces for efficient photoelectrocatalytic water splitting, Appl. Catal. B Environ. (2019) 118206, https://doi.org/10.1016/j.apcatb.2019.118206.
[13] J. Park, W. Yang, Y. Oh, J. Tan, H. Lee, R. Boppella, J. Moon, Efficient solar-to- hydrogen conversion from neutral electrolytes using morphology-controlled Sb2Se3 light absorbers, ACS Energy Lett. 4 (2019) 517–526, https://doi.org/ 10.1021/acsenergylett.8b02323.
[14] X. Wu, S. Asher, D.H. Levi, D.E. King, Y. Yan, T.A. Gessert, P. Sheldon, Interdiffusion of CdS and Zn2SnO4 layers and its application in CdS/CdTe polycrystalline thin-film solar cells, J. Appl. Phys. 89 (2001) 4564–4569, https:// doi.org/10.1063/1.1351539.
[15] H. Lim, D. Kim, M.-J. Choi, E.H. Sargent, Y.S. Jung, J.Y. Kim, Suppressing interfacial dipoles to minimize open-circuit voltage loss in quantum dot photovoltaics, Adv. Energy Mater. 9 (2019) 1901938. https://doi.org/10. 1002/aenm.201901938.
[16] A. Gankin, R. Sfez, E. Mervinetsky, J. Buchwald, A. Dianat, L. Medrano Sandonas, R. Gutierrez, G. Cuniberti, S. Yitzchaik, Molecular and ionic dipole effects on the electronic properties of Si-/SiO_2-grafted alkylamine monolayers, ACS Appl. Mater. Interfaces 9 (2017) 44873–44879, https://doi.org/10.1021/acsami.7b12218.
[17] R. Wick-Joliat, T. Musso, R.R. Prabhakar, J. Lockinger, S. Siol, W. Cui, L. S¨ ´every, T. Moehl, J. Suh, J. Hutter, M. Iannuzzi, S.D. Tilley, Stable and tunable phosphonic acid dipole layer for band edge engineering of photoelectrochemical and photovoltaic heterojunction devices, Energy Environ. Sci. 12 (2019) 1901–1909, https://doi.org/10.1039/C9EE00748B.
[18] C. Jiang, S.J.A. Moniz, A. Wang, T. Zhang, J. Tang, Photoelectrochemical devices for solar water splitting – materials and challenges, Chem. Soc. Rev. 46 (2017) 4645–4660, https://doi.org/10.1039/C6CS00306K.
[19] H. Kumagai, T. Minegishi, N. Sato, T. Yamada, J. Kubota, K. Domen, Efficient solar hydrogen production from neutral electrolytes using surface-modified Cu(In,Ga) Se2 photocathodes, J. Mater. Chem. A 3 (2015) 8300–8307, https://doi.org/ 10.1039/C5TA01058F.
[20] S. Akin, N. Arora, S.M. Zakeeruddin, M. Gratzel, R.H. Friend, M.I. Dar, New ¨ strategies for defect passivation in high-efficiency perovskite solar cells, Adv. Energy Mater. 10 (2020) 1903090. https://doi.org/10.1002/aenm.201903090.
[21] K. Choi, H. Choi, J. Min, T. Kim, D. Kim, S.Y. Son, G.-W. Kim, J. Choi, T. Park, A short review on interface engineering of perovskite solar cells: a self-assembled monolayer and its roles, Sol. RRL 4 (2020) 1900251, https://doi.org/10.1002/ solr.201900251.
[22] H. Imahori, H. Norieda, H. Yamada, Y. Nishimura, I. Yamazaki, Y. Sakata, S. Fukuzumi, Light-Harvesting and photocurrent generation by gold electrodes modified with mixed self-assembled monolayers of Boron− Dipyrrin and Ferrocene− Porphyrin− Fullerene triad, J. Am. Chem. Soc. 123 (2001) 100–110, https://doi.org/10.1021/ja002154k.
[23] Y. Yu, S.-C. Chien, J. Sun, E.C. Hettiaratchy, R.C. Myers, L.-C. Lin, Y. Wu, Excimer-mediated intermolecular charge transfer in self-assembled donor–acceptor dyes on metal oxides, J. Am. Chem. Soc. 141 (2019) 8727–8731, https://doi.org/10.1021/ jacs.9b03729.
[24] D. Bae, B. Seger, P.C.K. Vesborg, O. Hansen, I. Chorkendorff, Strategies for stable water splitting via protected photoelectrodes, Chem. Soc. Rev. 46 (2017) 1933–1954, https://doi.org/10.1039/C6CS00918B.
[25] S.-C. Yun, S. Ma, H.-C. Kwon, K. Kim, G. Jang, H. Yang, J. Moon, Amino acid salt- driven planar hybrid perovskite solar cells with enhanced humidity stability, Nano Energy 59 (2019) 481–491, https://doi.org/10.1016/j.nanoen.2019.02.064.
[26] C. Zhang, S. Zhang, X. Miao, Y. Hu, L. Staaden, G. Jia, Rigid amino acid as Linker to enhance the crystallinity of CH3NH3PbI3 particles, Part. Part. Syst. Charact. 34 (2017) 1600298, https://doi.org/10.1002/ppsc.201600298.
[27] O.S. Hutter, L.J. Phillips, K. Durose, J.D. Major, 6.6% efficient antimony selenide solar cells using grain structure control and an organic contact layer, Sol. Energy Mater. Sol. Cells 188 (2018) 177–181, https://doi.org/10.1016/j. solmat.2018.09.004.
[28] J. Tan, W. Yang, Y. Oh, H. Lee, J. Park, R. Boppella, J. Kim, J. Moon, Fullerene as a photoelectron transfer promoter enabling stable TiO2-protected Sb2Se3 photocathodes for photo-electrochemical water splitting, Adv. Energy Mater. 9 (2019) 1900179, https://doi.org/10.1002/aenm.201900179.
[29] L. Zhang, T. Minegishi, J. Kubota, K. Domen, Hydrogen evolution from water using AgxCu1− xGaSe2 photocathodes under visible light, Phys. Chem. Chem. Phys. 16 (2014) 6167–6174, https://doi.org/10.1039/c3cp54590c.
[30] D. Liu, L. Yang, Y. Wu, X. Wang, Y. Zeng, G. Han, H. Yao, S. Li, S. Zhang, Y. Zhang, Y. Yi, C. He, W. Ma, J. Hou, Tunable electron donating and accepting properties achieved by modulating the steric hindrance of side chains in A-D-A small- molecule photovoltaic materials, Chem. Mater. 30 (2018) 619–628, https://doi. org/10.1021/acs.chemmater.7b03142.
[31] H. Lee, E.H. Doud, R. Wu, R. Sanishvili, J.I. Juncosa, D. Liu, N.L. Kelleher, R. B. Silverman, Mechanism of Inactivation of γ-aminobutyric acid aminotransferase by (1S,3S)-3-amino-4-difluoromethylene-1-cyclopentanoic acid (CPP-115), J. Am. Chem. Soc. 137 (2015) 2628–2640, https://doi.org/10.1021/ja512299n.
[32] F. Buchbender, M. Wiese, Efficient concentration of an amino acid using reactive extraction coupled with bipolar electrodialysis, Chem. Eng. Technol. 41 (2018) 2298–2305, https://doi.org/10.1002/ceat.201800286.
[33] L. Cavallo, G. Guerra, P. Corradini, L. Resconi, R.M. Waymouth, Model catalytic sites for olefin polymerization and diastereoselectivity in the cyclopolymerization of 1,5-hexadiene, Macromolecules 26 (1993) 260–267, https://doi.org/10.1021/ ma00054a003.
[34] C. Melios, N. Huang, L. Callegaro, A. Centeno, A. Cultrera, A. Cordon, V. Panchal, I. Arnedo, A. Redo-Sanchez, D. Etayo, M. Fernandez, A. Lopez, S. Rozhko, O. Txoperena, A. Zurutuza, O. Kazakova, Towards standardisation of contact and contactless electrical measurements of CVD graphene at the macro-, micro- and nano-scale, Sci. Rep. 10 (2020) 1–11, https://doi.org/10.1038/s41598-020-59851- 1.
[35] W. Yang, J. Ahn, Y. Oh, J. Tan, H. Lee, J. Park, H.-C. Kwon, J. Kim, W. Jo, J. Kim, J. Moon, Water splitting: adjusting the anisotropy of 1d sb2se3 nanostructures for highly efficient photoelectrochemical water splitting, Adv. Energy Mater. 8 (2018) 1702888, https://doi.org/10.1002/aenm.201870061.
[36] J. Park, W. Yang, J. Tan, H. Lee, J.W. Yun, S.G. Shim, Y.S. Park, J. Moon, Hierarchal nanorod-derived bilayer strategy to enhance the photocurrent density of Sb2Se3 photocathodes for photoelectrochemical water splitting, ACS Energy Lett. 5 (2020) 136–145, https://doi.org/10.1021/acsenergylett.9b02486.
[37] Y. Zhou, L. Wang, S. Chen, S. Qin, X. Liu, J. Chen, D.-J. Xue, M. Luo, Y. Cao, Y. Cheng, E.H. Sargent, J. Tang, Thin-film Sb2Se3 photovoltaics with oriented one- dimensional ribbons and benign grain boundaries, Nat. Photonics 9 (2015) 409–415, https://doi.org/10.1038/nphoton.2015.78.
[38] C. Chen, Y. Zhao, S. Lu, K. Li, Y. Li, B. Yang, W. Chen, L. Wang, D. Li, H. Deng, F. Yi, J. Tang, Accelerated optimization of TiO2/Sb2Se3 thin film solar cells by high- throughput combinatorial approach, Adv. Energy Mater. 7 (2017) 1700866, https://doi.org/10.1002/aenm.201700866.
[39] L. Bertoluzzi, P. Lopez-Varo, J.A.J. Tejada, J. Bisquert, Charge transfer processes at the semiconductor/electrolyte interface for solar fuel production: insight from impedance spectroscopy, J. Mater. Chem. A 4 (2016) 2873–2879, https://doi.org/ 10.1039/C5TA03210E.
[40] J. Li, F. Li, J. Jin, Hole extraction and injection pathways constructed by the *in situ* growth of ultra-thin Fe-doped NiOOH Co-catalysts on a fluorine-doped α-Fe2O3 photoanode, J. Power Sources 482 (2021) 228957, https://doi.org/10.1016/j. jpowsour.2020.228957.
[41] L. Bertoluzzi, J. Bisquert, Equivalent circuit of electrons and holes in thin semiconductor films for photoelectrochemical water splitting applications, J. Phys. Chem. Lett. 3 (2012) 2517–2522, https://doi.org/10.1021/jz3010909.
[42] K. Sivula, F. Le Formal, M. Gratzel, Solar water splitting: progress using hematite ¨ (α-Fe2O3) photoelectrodes, ChemSusChem 4 (2011) 432–449, https://doi.org/ 10.1002/cssc.201000416.
[43] J. Tan, W. Yang, Y. Oh, H. Lee, J. Park, J. Moon, Controlled electrodeposition of photoelectrochemically active amorphous MoSx cocatalyst on Sb2Se3 photocathode, ACS Appl. Mater. Interfaces 10 (2018) 10898–10908, https://doi. org/10.1021/acsami.8b00305.
[44] W. Yang, S. Lee, H.-C. Kwon, J. Tan, H. Lee, J. Park, Y. Oh, H. Choi, J. Moon, Time-resolved observations of photo-generated charge-carrier dynamics in Sb2Se3 photocathodes for photoelectrochemical water splitting, ACS Nano 12 (2018) 11088–11097, https://doi.org/10.1021/acsnano.8b05446.
[45] K.-P. Wang, H. Teng, Zinc-doping in TiO2 films to enhance electron transport in dye-sensitized solar cells under low-intensity illumination, Phys. Chem. Chem. Phys. 11 (2009) 9489–9496, https://doi.org/0.1039/B912672D.
[46] D. Klotz, D.S. Ellis, H. Dotan, A. Rothschild, Empirical in operando analysis of the charge carrier dynamics in hematite photoanodes by PEIS, IMPS and IMVS, Phys. Chem. Chem. Phys. 18 (2016) 23438–23457, https://doi.org/10.1039/ C6CP04683E.
[47] D. Cardenas-Morcoso, A. Bou, S. Ravishankar, M. García-Tecedor, S. Gimenez, J. Bisquert, Intensity-modulated photocurrent spectroscopy for solar energy conversion devices: what does a negative value mean? ACS Energy Lett. 5 (2020) 187–191, https://doi.org/10.1021/acsenergylett.9b02555.
[48] P. Zhai, S. Haussener, J. Ager, R. Sathre, K. Walczak, J. Greenblatt, T. McKone, Net primary energy balance of a solar-driven photoelectrochemical water-splitting device, Energy Environ. Sci. 6 (2013) 2380–2389, https://doi.org/10.1039/ C3EE40880A.
[49] Y. Xue, W. Dong, X. Wang, W. Bi, P. Zhai, H. Li, M. Nie, Degradation of sunscreen agent *p*-aminobenzoic acid using a combination system of UV irradiation, persulphate and iron(II), Environ. Sci. Pollut. Res. 23 (2016) 4561, https://doi. org/10.1007/s11356-015-5631-z.